INSTITUTE OF PHYSICS PUBLISHING NANOTECHNOLOGY
Nanotechnology **16** (2005) 3101–3109 doi:10.1088/0957-4484/16/12/063

Tailored transport through vertically aligned carbon nanofibre membranes; controlled synthesis, modelling, and passive diffusion experiments

J D Fowlkes[1,2,4], B L Fletcher[1], E D Hullander[1], K L Klein[1,2], D K Hensley[1], A V Melechko[1,2], M L Simpson[1,2] and M J Doktycz[1,3]

[1] Molecular-Scale Engineering and Nanoscale Technologies Research Group, Condensed Matter Sciences Division, Oak Ridge National Laboratory, PO Box 2008, MS 6006, Oak Ridge, TN 37381-6006, USA
[2] Materials Science and Engineering Department, The University of Tennessee, Knoxville, TN 37996-2200, USA
[3] Life Sciences Division, Oak Ridge National Laboratory, PO Box 2008, MS 6123, Oak Ridge, TN 37831, USA

E-mail: jfowlkes@ornl.gov

Received 24 June 2005, in final form 30 September 2005
Published 11 November 2005
Online at stacks.iop.org/Nano/16/3101

Abstract
The ability to control the permeability of a synthetic membrane structure formed by a spatially stochastic forest of vertically aligned carbon nanofibres is demonstrated. Control of membrane pore size and morphology was achieved by varying the thickness of a uniform, conformal coating of SiO_2 on the nanofibre surfaces. Characterization of passive diffusion using fluorescence microscopy and labelled latex beads confirms the ability to alter membrane permeability. Further, statistically reproducible transport regimes are predicted for the spatially stochastic membrane as a function of the nanofibre diameter by a Monte Carlo simulation technique. Realizing predictable nanoscale behaviour in a microscopically random, statistical structure is essential for applications requiring controlled, species specific transport.

1. Introduction

Biological cells perform a vast array of functions. These functional attributes are enabled by the physical size of the cell and the spatial organization of its chemical constituents. For example, the small physical size of the cell (typically less than 100 μm), and its component substructures, facilitate diffusion-based transport and mixing. A thin, nanoscale-featured membrane encompasses the cell to define its volume and to control the transport of materials. Emulating such multiple length scale features in synthetic devices will be essential for realizing the engineering advantages of natural cells. This will require the creation of cell mimic structures that are able to contain small volumes of reagents using synthetic membranes with nanoscale elements.

Synthetic membrane structures have been fabricated in silicon using various micro- and nano-engineering techniques. Such structures lack the fluidity of natural lipid bilayer membranes. However, this approach to construction exploits mature fabrication processes, allows precise engineering across multiple length scales and enables interfacing to electronic and optical components. Further, the rigidity of these structures permits robust operation and long-term storage when compared to polymer- or lipid-bilayer based membranes. A host of fabrication techniques have been used to construct synthetic membranes including surface micromachining [1],

[4] Author to whom any correspondence should be addressed.

laser interference lithography [2], nanoimprint lithography [3], track etching [4], backside etching [5] and phase separation [6].

Vertically aligned carbon nanofibre arrays (VACNFs) [7–12] can also be used to create synthetic membranes. VACNFs are deterministically grown by plasma-enhanced chemical vapour deposition (PECVD) and can be combined with silicon micromachining techniques to create cell mimic structures [13] and microfluidic devices [14]. As illustrated in figure 1, the VACNFs can be used to confine reagents within a microscale volume. The nanofibres constituting the membrane are aligned perpendicular to the transport direction and are exploited as size-selective permeable membranes. Photolithographic-based definition of the membrane combined with the controlled synthesis of nanofibre elements exemplifies engineering across multiple length scales [13]. The size exclusion properties of the membrane depend on the diameter and placement of the VACNFs. When VACNFs are grown from a thin, continuous film of catalyst, a random arrangement of nanofibres is created. The resulting membrane structure has been shown to exclude latex beads larger than 500 nm in diameter and restrict transport of smaller beads [13]. A fabrication challenge will be the further refinement of the membrane characteristics, requiring additional control of the physical and chemical properties of the carbon nanofibres.

In addition to challenges in fabrication, a second significant challenge is characterization of the membrane transport characteristics. These include the length of time involved in conducting diffusion experiments and the limitations in correlating microscopic membranes with nanoscopic behaviour [15]. Various techniques have been applied to characterize membrane transport including the mercury intrusion method [16], the bubble point method [17], electrical conduction [15], and the size exclusion method [13]. Computer simulation can also be an effective tool to characterize membrane transport. Monte Carlo simulations have been applied to various diffusive transport problems in sieving matrices [18–26]. Considering the parallel challenges in fabrication, this approach can provide a necessary tool for identifying appropriate experimental conditions and for designing structures for particular applications.

In this paper, the ability to specifically tailor the pore size of VACNF-based membranes by depositing a conformal coating of SiO_2 is presented. PECVD proved to be a reproducible technique to uniformly coat SiO_2 on the surface of a forest of carbon nanofibres. This technique increased the average nanofibre diameter, leading to a decrease in the average pore size. This not only alters the exclusion limits of the membrane but also leads to nonlinear transport behaviour as a function of conformal coating thickness. Computer simulation techniques are used to understand this transport behaviour. Specifically, a Monte Carlo based simulation is employed to replicate the physical structure of the membrane barrier as well as to simulate the random walk transport of species through this barrier.

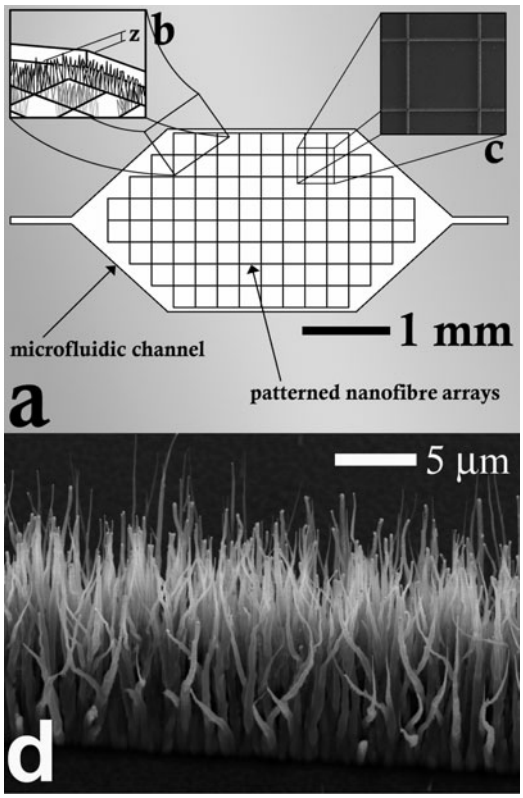

Figure 1. (a) A top-down schematic illustration of the cell mimic device. The portion of the device in white represents the microfluidic channel which is etched typically 8–10 μm into the substrate surface. The interconnected cell mesh is formed by a patterned array of VACNFs. (b) The tilted illustration shows that the nanofibres are grown to extend above the initial substrate surface, typically 4–8 μm. (c) An FESEM image of a cell following VACNF growth. Following this step, the individual cells of the device are filled with the molecules of interest and the device is sealed by applying a rigid, transparent lid to the top of the device. A transparent, viscous polymer is applied to the underside of the lid prior to sealing, into which the tips of the carbon nanofibres imbed. This completely seals off the device from the surrounding environment; cell-to-cell communication occurs via the nanoscale pore space between individual nanofibres constituting the membrane. The thin channels extending from the ends of the device are fluid access points to provide media to the cells. (d) The nanofibre membrane barrier viewed at $\theta = 35°$ from the substrate surface normal. A PDMS-coated, glass slide lid was later used to seal the top portion of the nanofibre barrier and prevent bead diffusion over the membrane barrier effectively restricting bead transport via the interfibre space.

2. Experimental details

2.1. Vertically aligned carbon nanofibre (VACNF) growth

The carbon nanofibre forest nucleates and grows from an initially continuous Ni catalyst pattern during the PECVD growth process. A thin 50 nm Ni film acts as a catalyst for the growth of the stochastic carbon nanofibre forest. In the first stage of the growth process, the continuous Ni film is converted into a random array of Ni nanoparticles in response to a DC plasma etch (100 mA) in 80 sccm NH_3 (3 mTorr) at an elevated temperature of 700 °C. A combination of etching and annealing leads to the formation of the nanoparticle film morphology. Carbon nanofibre growth ensues at the discrete location of each catalyst particle with the introduction of 55 sccm acetylene (C_2H_2) to the NH_3 atmosphere. The acetylene decomposes in the plasma at the Ni nanoparticle catalyst sites, diffuses to the base of the nanoparticle and

condenses there in the form of tapered, graphene sheets. Subsequent graphene layers grow in a layer by layer fashion lifting the catalyst nanoparticle off the substrate surface forming a carbon nanofibre. The thickness of the Ni catalyst film inevitably controls the morphology of the nanofibre forest. Thicker catalyst films yield larger nanoparticles, increasing the average spacing between individual nanoparticles as a function of increased film thickness [12]. This interfibre space acts as the permeable constituent of the nanofibre membrane. Additional detail on VACNF growth and applications can be found in [27].

2.2. SiO_2 deposition on VACNFs

A SiO_2 conformal sheath was grown on VACNF membrane structures by the PECVD technique. An Orion thermal PECVD manufactured by Trion Technologies was used to deposit the SiO_2 from NO_2 ($Q_{NO_2} = 125\ cm^3\ min^{-1}$) and SiH_4 ($Q_{SiH_4} = 125\ cm^3\ min^{-1}$) precursor gases. The films were deposited at 400 °C in 1 Torr of the precursor gas mix. A variable growth time ranging from $t = 1$ to 30 min was used to vary the thickness of the SiO_2 coating on the nanofibres. The conformal sheath exhibited a linear growth rate of $v = 0.75\ nm\ s^{-1}$ over the entire time range studied. The growth rate of the oxide on the carbon nanofibres was roughly half of the magnitude of the growth rate on the surrounding, flat Si wafer surface. This was attributed to the combination of the large surface area of the membrane barrier and interaction of the barrier structure with the transport of precursor gases.

2.3. Passive diffusion experiments

Fluoresbrite YG carboxylate microspheres (2.5% solids-latex, $d = 32 \pm 8$ nm, Polysciences) were deposited into individual cell mimic structures using a piezo inkjet nozzle (MicroFab Technologies). A 50 μm diameter inkjet nozzle deposited a ~100 pl reagent volume into the structures. The microspheres were suspended in a solution containing 1:1 glycerol:H_2O; the glycerol kept the microspheres suspended in solution, prevented them from sticking to the Si substrate and prevented the rapid drying of the droplet. Moreover, prior to the inkjet step a blocking solution containing 1% v/v of 1:10 sodium dodecyl sulfate (SDS) in H_2O, 50% of 1:50 albumin, bovine (96–98% pure) in H_2O, and 49% phosphate buffered saline (PBS, 0.1 M sodium phosphate, 0.15 M sodium chloride, in 500 ml deionized H_2O, pH 7.5) further prevented beads from sticking to the Si surface. The base of the cell mimic structure consisted of a flat Si wafer which was coated with a PECVD SiO_2 along with the membrane structure.

The structure was sealed by applying a polydimethylsiloxane (Sylgard 182 PDMS, Dow Corning) coated glass slide atop the entire cell mimic structure as described previously [13]. The transparent glass slide facilitated characterization by fluorescence microscopy. The tips of the nanofibres embed into the soft, PDMS layer creating a floor to ceiling barrier, sealing off individual cells from adjacent ones. Microfluidic channels, 50 μm wide $\times 10$ μm deep, extend beyond the sealed area of the structure so that a buffered solution may be introduced into the structure to wet the cells. Again, PBS was used for this purpose. Once the structure was wetted with PBS, fluorescence microscopy images were taken periodically (over the course of days) to image the progress of bead diffusion within the confines of the cell, as well as beyond the nanofibre membrane barrier, to determine the pore size property of the membrane barrier.

2.4. Monte Carlo simulation of the cell mimic device and passive diffusion

The VACNF membrane barrier structure was reproduced computationally by obtaining the average diameter, height, surface density, and tilt of the SiO_2–carbon nanofibre composites from a sufficient number of FESEM images to calculate a statistically relevant average and standard deviation for each variable. These values were then used as input into a simulation which used Monte Carlo principles to replicate the random behaviour of these variables and produce a simulated cell mimic structure. An average nanofibre diameter of $d = 182 \pm 56$ nm and an average nanofibre surface density of $\rho_{fibre} = 2.5$ fibre μm^{-2} was determined from FESEM images following the fibre growth process. The average nanofibre diameter was calculated by measuring the nanofibre diameter for a large number ($n = 110$) of nanofibres from a series of FESEM images taken over several cell mimic devices on the same Si wafer. The nanofibre surface density was measured by superimposing a square box (2 μm $\times$ 2 μm) over the centre of the 5 μm wide catalyst strip and counting the number of nanofibres within the confines of the box. This procedure was also carried out over a statistically significant number of FESEM images (nine different images sampled from random locations over three different cell mimic structures).

Three-dimensional, passive diffusion simulations were also conducted to assess the transport response of the membrane barrier as a function of nanofibre diameter. The simulation was written and compiled using the Matlab programming language available from The MathWorks. Care was taken to replicate both the geometry of the cell mimic structure and the initial conditions for simulating actual diffusion experiments, e.g., a hemispherical concentration of beads in the centre of the cell at $t = 0$ s to mimic the inkjet dispensing. The simulation was carried out for carbon nanofibres with $h = 5$ μm tall and a square cell dimension of 50 μm that defines a cell volume of 12.5 pl. A total of 3257 beads, in a hemispherical volume of 50 fl, was centred on the cell floor. Each bead was allowed to jump one pixel per cycle based on the random walk model of atomic diffusion. This cyclical process was repeated until the permeability of the membrane was characterized spatially and temporally.

3. Results and discussion

3.1. SiO_2-coated, vertically aligned carbon nanofibres

Figure 1(d) shows an FESEM image of the VACNF barrier where the substrate has been tilted at $\theta = 35°$ with respect to the substrate surface normal vector to highlight the interfibre spacing of the membrane barrier. *The porous, void network in the interfibre space is partially apparent in the image and appears as the dark regions intermixed within the first row of nanofibres*. The voids appear dark in the image because there is no secondary electron emission from the unoccupied

Table 1. A list of the relevant VACNF structure parameters required to simulate real VACNF structures fabricated with various SiO_2 coating thicknesses. These same values were used as input into the Monte Carlo simulation to generate a replica structure for simulating passive diffusion by a random walk process.

t (s)	Fibre diameter, D (nm)	ΔD (nm)	Fibre density, ρ (fibres μm^{-2})	Fibre tilt θ (deg)	Membrane width W (μm)	Fibre height h (μm)	Δh (μm)
0	182	56	2.2	20	5	18	2.5
300	580	110	2.2	20	5.4	18	2.5
600	986	159	2.2	20	5.8	18	2.5

space. The total length of the void channel through the barrier can be determined by fracturing the membrane barrier followed by FESEM analysis. It should be emphasized that understanding the transport characteristics of the membrane barrier depends on understanding the spatial distribution of the nanofibres and the resulting networks of porous channels. Table 1 lists the geometrical attributes including nanofibre diameter, height, tilt, and density derived from several replicate structures. These features ultimately determine the porosity of the membrane. The heights of the carbon nanofibres exhibit a statistical deviation about an average where the mean height of the carbon nanofibres was measured at $h = 18.0 \pm 2.5$ μm. This height variation is apparent in figure 1(d). It is important that all the nanofibres extend above the initial substrate surface to completely seal the device. When the cell structure is improperly sealed from the top, large channels are created just beneath the lid surface. Unrestricted diffusion of beads ensues at these locations, bypassing the interfibre porous membrane channels. This is undesirable and can extend the cycle time between structure design and experimental evaluation if improperly sealed.

A conformal, silicon dioxide (SiO_2) coating was grown on the nanofibres of the membrane barrier in order to alter the effective membrane pore size. Figure 2 illustrates a collage of FESEM images of nanofibre barriers coated with various SiO_2 sheath thicknesses. The sheath thickness increases linearly with increasing oxide growth time ($v = 0.75$ nm s^{-1}). The images in figure 2 further illustrate that the oxide sheath is grown simultaneously on the nanofibres by the PECVD process. Further, a uniform, conformal *nanoscale* coating is produced over *microscopic* dimensions. For example, the SiO_2 layer was found to deposit uniformly over the entire surface of individual nanofibres. SiO_2-coated VACNF membranes were fractured to better evaluate the consistency of the SiO_2 coating along the entire length of individual carbon nanofibres. This fracture technique resulted in a fraction of the nanofibres being displaced onto the interior portion of the cell mimic chip, lying on their sides, enabling FESEM viewing of the SiO_2 layer over the entire length of the nanofibre. The SiO_2 layer was found to coat the nanofibres in a conformal fashion. In fact, small 50–100 nm protrusions observed on the surfaces of uncoated VACNFs were buried within the SiO_2 coating for coated nanofibres with diameters >500 nm. The elevated temperature during SiO_2 growth ($T = 400$ °C) coupled with the slow SiO_2 growth rate ($v = 0.75$ nm s^{-1}) produced the evolution of a smooth surfaced, cylindrical nanopillar; the minimum surface area configuration possible for a high-aspect-ratio feature. *Such uniform and simultaneous deposition translates into the desired result of a homogeneous reduction in pore size over the entire membrane structure.*

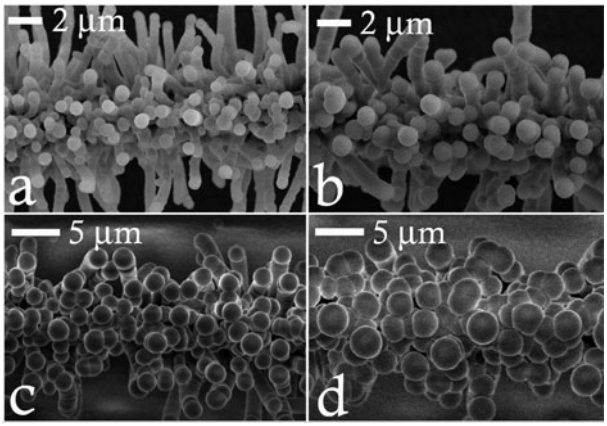

Figure 2. The morphology of the SiO_2 coated nanofibre membrane barrier following (a) $t = 360$ s, (b) $t = 600$ s, (c) $t = 1200$ s, and (d) $t = 1800$ s of PECVD growth of the conformal oxide layer with (a) $r = 260$ nm, (b) $r = 400$ nm, (c) $r = 860$ nm, and (d) $r = 1370$ nm, where r is the thickness of the conformal, oxide sheath around the circumference of the carbon nanofibres. The thickness of the oxide coating exhibits a linear relationship with growth time.

3.2. Passive diffusion experiments

Passive diffusion control experiments were first performed on cell mimic structures with a membrane barrier composed of *uncoated* VACNFs. The average interfibre spacing for the uncoated nanofibres was calculated to be 590 nm, which represents a rough estimate of the average pore size since the measurements were made between the closest *surfaces* of first nearest neighbour nanofibres and not between their *central axes*. These measurements were made using FESEM image analysis by viewing the nanofibre membrane forest at normal incidence. This measurement may also be considered the minimum, critical pore dimension since the pore dimension parallel to the length of the nanofibres is expected to be elongated. A bead size was selected ($d = 320$ nm) that had a diameter less than 590 nm so that the beads can easily permeate the membrane barrier. Fluorescence microscopy was used to monitor the diffusion of the beads as a function of time. The images presented in figure 3 show the fluorescently labelled latex beads shortly after inkjet dispensing into the centre of the cell (figure 3(a)) and roughly four days after the cell was wetted with PBS buffer solution to facilitate bead diffusion (figure 3(b)). The images were taken normal to the substrate surface and through the glass slide lid; the structures were wetted and sealed when the images were acquired. The images presented in figure 3(b) show that after ~4 days, under passive diffusion conditions, the beads

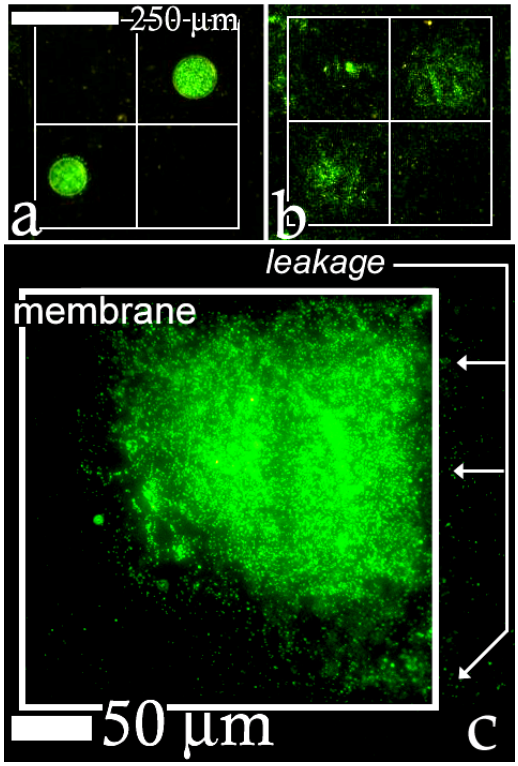

Figure 3. (a) A fluorescence micrograph following bead dispensing into two adjacent cell mimic structures. The nanofibres of the membrane were uncoated for this experiment. The structures were subsequently sealed and a buffer solution allowed to flow into the cells by way of microfluidic channels providing a media for bead diffusion in the cell. The fluorescence micrograph shown in (b) was taken after 4 days. The pore size for the uncoated carbon nanofibres in the cell membrane boundary allowed for the unimpeded diffusion of $d = 321 \pm 8$ nm beads. The interfibre space was characterized as having an average nanofibre diameter of $d = 182 \pm 56$ nm and an average interfibre spacing of $s = 590 \pm 200$ nm. (d) A fluorescence image of $d = 321 \pm 8$ nm fluorescently labelled latex beads mostly contained within a cell mimic structure with the membrane characteristics of $d = 986$ nm SiO_2 coated, carbon nanofibres with an average interfibre spacing of $s = 290 \pm 100$ nm. The collective area occupied by the latex beads outlines a portion of the square cell due to the confinement of the diffusing beads by the oxide coated nanofibres. The small and finite number of interfibre pores that are larger than the bead size limits the number of beads that escape the structure; beads leak from the structure most prominently from the lower right-hand corner of the mimic shown ($t = 6$ days).

permeated the uncoated nanofibre barrier and transferred into adjacent, unpopulated cell structures. Closer examination of figure 3(b) shows that the bead concentration gradient within the cell did not reach equilibrium $\nabla C(x, y) \neq 0$ prior to the diffusion of beads through the membrane. Had this been the case the outline of the cell membrane barrier would be evident in the fluorescence image as the cell would be filled nearly homogenously throughout with latex beads forming a virtual green square. Instead, before the cell can homogeneously fill, beads have already permeated the barrier diffusing into the confines of adjacent cells as well as a number of beads having dropped out of a solution suspension adhering to the bottom of the cells. Observation of the wetting process confirms this (data not shown). Figure 3(c) shows the results for the case of a less permeable, SiO_2-coated membrane, where the beads are mostly confined to the interior of the cell. This confirms the ability to control transport by SiO_2 coating of the membrane. In fact, a fluorescent image of the membrane barrier is delineated on one side of the cell by the diffusing fluorescent beads in the cell interior. Nevertheless, containment of the bead population is incomplete. In the bottom, right corner of the image in figure 3(c), a few beads have permeated through the membrane, thereby escaping the interior of the cell mimic. A rough estimate of the average pore size of this membrane yields a value of 290 nm. This value is less than the bead size and would be expected to contain the beads. However, the standard deviation of this average was ±100 nm. Thus, it would be expected that pores as large as 390 nm are possible for this membrane, allowing some of the beads to escape the structure. This example illustrates the statistical nature of stochastic structures.

In order to test fully the containment potential provided by SiO_2-coated nanofibres a membrane was exposed to an excessive PECVD growth time ($t > 30$ min) in an attempt to seal the cell mimic from the surrounding environment. Latex beads of 50 nm diameter were dispensed into the cell mimic structure prior to sealing the device. The PBS buffer solution introduced into the cell mimic device was unable to permeate the nanofibre barrier to wet the internal region of the cell. After several days the 50 nm beads dropped out of the inkjet suspension droplet without ever wetting the cell mimic device. Hence, sealing of the structure so as to prevent wetting is possible with thick oxide coatings.

3.3. Non-linear transport and Monte Carlo simulation

The flux through the nanofibre membrane is expected to scale inversely with nanofibre diameter; as the nanofibre diameter increases the effective pore space among the nanofibres is reduced. However, structural attributes of the SiO_2-coated nanofibres were identified that were expected to produce a *non-linear* dependence of the transport as a function of the SiO_2-coating thickness. For example, the nanofibre density was found to *decrease* as the diameter of the nanofibre *increased*. The decrease in nanofibre surface density was attributed to the merging of SiO_2-coated nanofibres during the growth process to form even larger cylindrical aggregates, as is shown in figure 4. Figure 4 shows that individual nanofibres not only merge to form larger aggregates but these aggregates also change shape to form cylindrical posts. The collage of FESEM images shown in figure 4 was assembled from a collection of experiments conducted at different oxide growth times; each of the seven individual cell mimic structures was derived from the same Si wafer so that the underlying VACNF scaffold had the same nanofibre density and diameter distribution for each experiment. In addition, the overall width of the membrane increases as nanofibre diameter increases. For example, the membrane width increases by a factor of $2 \times r$ when a conformal coating is deposited on the nanofibres, where r is the thickness of the coating.

The coupled change in nanofibre density and membrane width made a simple linear extrapolation of the transport behaviour of the SiO_2-coated membranes inaccurate. Hence, a Monte Carlo based simulation was created to replicate the

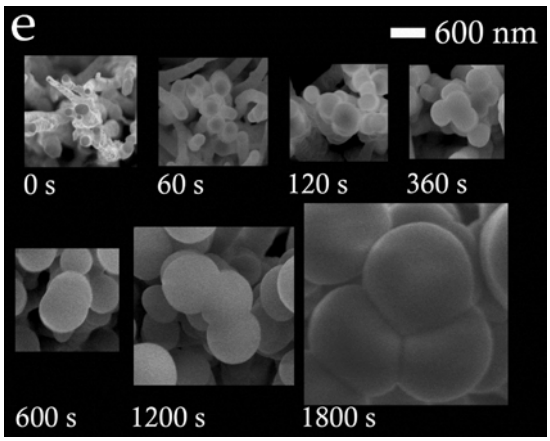

Figure 4. SiO_2-coated nanofibres merge into larger aggregates as oxide growth time increases. The image shows the effective reduction in the nanofibre density as nanofibres first individually thicken ($t = 60$ and 120 s) and then merge to form larger cylindrical aggregates ($t = 360$–1800 s).

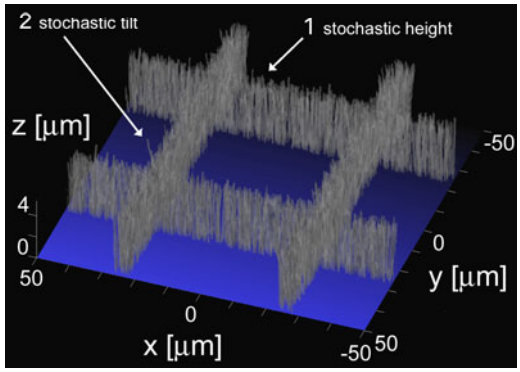

Figure 5. A Monte Carlo based computer simulation was used to generate a virtual replica of the cell mimic structure, paying particular attention to the cell mimic geometry and the stochastic nature of the nanofibre barrier. In this instance a nanofibre density of 1.2 fibres μm^{-2} was randomly generated with an average SiO_2–carbon nanofibre diameter of 800 nm. The random nature of the simulated height (1) and tilt (2) is indicated in the image where these features are most evident.

SiO_2-coated nanofibre morphology, including such variables as nanofibre shape, density, conformal oxide growth, and tilt. Additionally, the random nanofibre placement within the cell mimic structure was reproduced to simulate the geometry of the cell mimic structure as well as the membrane morphology. SiO_2 coated nanofibres were also reproduced to merge in the fashion previously shown in figure 4 to simulate real membrane structure. The Monte Carlo aspect of the code was used to replicate the stochastic nature of the nanofibre membrane barrier observed in each of the aforementioned variables experimentally. For example, figure 2(d) exemplifies the random tilt, diameter, and density observed in real VACNF membrane structures. Figure 5 shows an example of a simulated cell mimic structure calculated by this Monte Carlo based scheme and exhibits the parameter range for each of these variables. The computer generated cell mimic in figure 5 was generated using a nanofibre density of 1.2 nanofibres μm^{-2} and a SiO_2–carbon nanofibre composite diameter of 800 nm. These specific parameters best illustrate the random nature of the structure and the pores between the nanofibres. The actual parameters used to simulate experimental conditions are summarized in table 1.

A Monte Carlo simulation was also applied to simulate the random walk of beads in the cell mimic structure for several cases including conditions similar to the experiments presented in figures 3(a), (b) and (c). The Monte Carlo simulation predicts the transport through the nanofibre membrane as a function of nanofibre diameter and elucidates the various regimes of transport. The complete range of possible membrane morphologies from uncoated nanofibres to entirely sealed cell structures was evaluated.

The simulation indicates four regimes of membrane transport behaviour which are defined here, for convenience, as *open*, *restricted*, *leaky*, and *closed* regimes. In an *open* regime, diffusion ensues as if a barrier structure did not exist. The uncoated nanofibre membrane exhibits transport behaviour characteristic of this regime (figure 6(a)). For a structure with a 400 nm thick layer of oxide per nanofibre, a *restricted* regime ensues where significant bead–nanofibre interaction occurs and the membrane controls the spatial release of beads (figure 6(b)). The membrane exhibits a collective, uniform permeability in this regime. The *restricted* regime is especially attractive for controlled release applications due to the homogeneous release of species through the barrier. The stochastic distribution of nanofibres leads to localized flaws in the membrane structure when the interfibre pore size is on the order of the bead diameter (figure 6(c)). In this *leaky* regime, where the oxide coating thickness is 800 nm and the line density of pores is 0.01–0.1 pores μm^{-1} of barrier, asymmetric spatial leakage typically occurs, producing the localized release of beads from the cell. A *closed* barrier forms when $d = 1.1$ μm for the SiO_2–nanofibre composite.

The simulation proved a valuable tool for predicting the minimum PECVD growth time required for confining the entire bead population while still allowing transport of fluid or smaller species. This is an important capability because the minimum coating thickness that allows containment, whilst still allowing the flow of solution through the membrane, must be arrived at precisely. This would be especially useful for the containment of large species while exchanging smaller reagents. Moreover, the simulation proved applicable over the range from uncoated nanofibres to sealed structures. For example, the predicted bead concentration profiles in figures 6(a) and (c) agree remarkably well with the experimental results presented in figures 3(a), (b) and (c), respectively. In addition, a search routine was compiled within the simulation code to scan and detect regions of the membrane barrier that facilitated bead transport in order to generate a 3D map of the porosity of the SiO_2-coated membrane in this region. Knowledge of the internal size and morphology for the nanoscale pore channel network introduces new possibilities for the function of the membrane such as the control of transport by particle–pore surface interaction.

Figure 6 illustrates the different pore channel morphologies that result from changing the thickness of the oxide layer surrounding individual nanofibres. The pore structure consists of interconnected and overlapping channels forming a complex

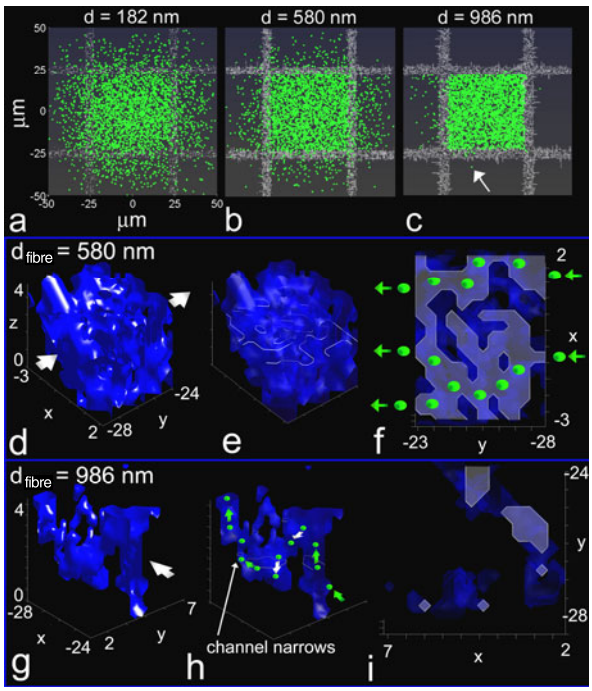

Figure 6. Simulations of passive bead diffusion for (a) uncoated nanofibres ($d = 182$ nm), (b) nanofibres coated for $t = 300$ s with SiO_2 ($d = 580$ nm), and (c) for $t = 600$ s ($d = 986$ nm). The uncoated nanofibres contributed very little resistance to the flow of beads. Near complete bead containment within the confines of the cell was achieved for a barrier consisting of fibres with $d = 986$ nm. Reference is made to the arrow in the discussion below. A 3D image of the simulated membrane pore morphology for a defect in a membrane consisting of (d)–(f) a membrane consisting of nanofibres of diameter 580 nm and a membrane (g)–(i) consisting of $d = 986$ nm nanofibres. Images (d) and (g) illustrate the 3D structure of the pore morphology where the blue surface represents the open volume of the pore. The superimposed arrows represent the direction of transport through the membrane. The same image is displayed in the images presented in (e) and (h); however, a transparency gradient has been applied to the images with a vertical contour slice at one z-value to add visual perspective to the 3D image. In images (f) and (i) the isosurface has been sheared off above this plane to display a cross-section through the pore morphology and this is shaded as transparent grey in the image. The superimposed bead illustration was used to emphasize the contorted, 3D path required for bead transport in the channel structure shown in image (h); the green arrows indicate upward motion while the grey arrows indicate downward motion. Transport across the membrane shown in (f) was planar due to the density of accessible pore space.

weave of interfibre space for a nanofibre membrane containing nanofibres with a diameter of 580 nm where a *restricted* type transport regime is observed both experimentally and computationally (figures 3(a), (b) and 6(b)). The pore structure is akin in morphology to an overlapping mass of pasta noodles. Although the nanofibres are largely vertically aligned, the stochastic nanofibre spacing and tilt can lead to tortuous paths through the membrane. Moreover, the effective cross-section of the pore complex (figure 6(f)) provides enough diffusive pathways such that at least one pathway for transport will allow the passage of $d = 320$ nm beads. Diffusion through the pore complex can occur in the 2D cleaved plane without the need for moving in the z-direction to pass through the membrane.

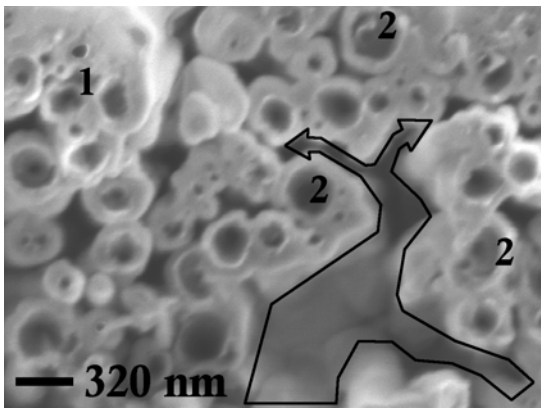

Figure 7. An FESEM image of a fractured membrane consisting of $d = 580$ nm nanofibres. Both experiment and simulation showed the transport of $d = 320$ nm beads (see scale bar) through the membrane structure occurred. The unfilled arrow path indicates a continuous pathway through the membrane that could transport beads of this size. The feature labelled with 1 is a particularly wide nanofibre and an unfavourable pathway for transport. The features labelled with 2s extend much higher than surrounding features, following the fracture procedure.

The case is quite different however for a more dense nanofibre membrane. Figure 6(g) shows a 3D section of membrane for a nanofibre forest consisting of thicker nanofibres ($d = 986$ nm). In this instance, the pore morphology consists of a single elongated and twisting channel that is significantly constricted in dimension relative to the pore complex observed for the other examined membrane fragment. In fact, a pinched neck exists near the end of the pore channel that can significantly impede bead transport (arrow in figure 6(h)). Therefore, a host of factors determine bead transport, including pore channel length, pore diameter, the bead concentration gradient across the pore, and the membrane barrier width. These variables are strongly coupled and interact to define the four regimes of transport listed previously.

The simulated pore morphology was compared with the real pore network of the membrane barrier by acquiring FESEM images of a fractured membrane to determine if the simulation accurately predicted this tortuous morphology. Figure 7 shows a FESEM image of a fractured membrane viewed along the vertical axis of the nanofibres. The nanofibres protruding above the cell mimic channel were fractured by simply dragging a razorblade across a cell mimic structure. The nanofibres fractured unevenly, leading to a textured cross-section rather than a perfectly smooth planar section. For example, the regions labelled by the numeral 2 in the image extend higher vertically relative to other locations in the image. However, the depth of field of the FESEM probe far exceeds in magnitude the height of the nanofibres, so even a nanofibre that has been cleaved at its base will appear as a stump in the image. Thus, VACNF membranes exhibiting the 2D transport behaviour characteristic of *open* or *restricted* regimes (figure 6(f)) may be identified. The FESEM image (figure 7) shows a particularly porous region (unfilled arrow superimposed on the image) in the membrane structure expected to allow the transport of 320 nm beads. The average nanofibre diameter for the membrane shown was

580 nm and thus the image can be compared with the modelling results presented in figure 6(d)–(f). The simulation (figure 6(f)) predicted such interconnected, >320 nm pore channels, within the membrane barrier. The nanofibre conglomerate labelled by the numeral 1 in the image is a dense region in the membrane which would be expected to impede transport. This nanofibre 'bundle' was formed by the aggregation of multiple nanofibres during the oxide growth process: a phenomenon that was referred to previously in figure 4.

Structures identified as *leaky* deliver a non-uniform dose along the length of the membrane (figure 6(c)). Comparison of this transport regime with the nanofibre membrane morphology reveals that the observed non-uniform transport correlates with (1) a reduced pore diameter/longer pore channel (figures 6(g)–(i)) coupled with (2) a non-uniform density of pores per unit length of membrane. As an example of point (1), the operative pore shown in figure 6(g), which allowed for the transport of the bead indicated in figure 6(c) by the superimposed arrow, had a pinched region along the pore channel with a diameter equal to roughly the bead diameter and a total channel length greater in magnitude than the width of the membrane. In addition, with reference to point (2), this was the only pore that mediated transport across this edge of the specified square cell membrane; however, it was not the only trans-membrane pore. Additional pores that traversed the membrane had pinched portions with cross-sections smaller than the bead size and hence could not support transport. Such pores are characteristic of *leaky* membranes.

Defining structures that permit restricted transport of specific particle sizes will require stringent control of the PECVD oxide growth process. Alternatively, the nanofibre patterning and growth process can be improved. A reduction in the deviation in VACNF morphology parameters such as the nanofibre diameter and tilt could reduce variables attributed to the stochastic nature of the nanofibres. A new VACNF growth chamber has been built which addresses this problem by providing more precise control over the nanofibre growth process. The discrete patterning of individual VACNFs by electron beam lithography would reduce variations in nanofibre density and would inevitably lead to a more uniform spatial distribution of pores per unit length of membrane. Increasing the width of the nanofibre barrier is another possible pathway to reduce the deviation in membrane transport behaviour by simply increasing the number of nanofibres contributing to the average thereby reducing the statistical nature of the structure. However, such an approach leads to a decrease in transport across the membrane due to the increase in pore channel length. Future work coupling experiment and simulation will evaluate these proposed avenues to control molecular scale permeability through such VACNF membranes.

4. Conclusions

A SiO_2 conformal sheath was grown on stochastic VACNF membrane structures by the PECVD technique. The conformal, silicon dioxide coating layer was grown on the nanofibres constituting the membrane barrier in order to control the effective pore size. The resulting multi-length scale processing translated into the desired result of a reduction in the average pore size over the entire membrane structure. Passive diffusion experiments were performed to test the effect the SiO_2 coated nanofibres had on membrane transport. The permeability property of the VACNF barrier was found to be controllable by varying the thickness of the oxide coating. Further, various transport regimes were predicted for the spatially stochastic membrane as a function of the nanofibre diameter by a Monte Carlo modelling technique. These regimes were related to the change, on the nanoscale, of the size, length and morphology of individual pores. A restricted transport regime was identified where a spatially uniform flux of species was emitted from the cell mimic structure. Such transport is crucial for the application of the cell mimic devices in controlled release applications.

Acknowledgments

This research was supported by NIH grant EB000657 and the Material Sciences and Engineering Division Program of the DOE Office of Science. This work was performed at the Oak Ridge National Laboratory, managed by UT-Battelle, LLC, for the US DOE under contract No DE-AC05-00OR22725.

References

[1] Desai T A, Hansford D and Ferrari M 1999 *J. Membr. Sci.* **159** 221
[2] van Rijn C J M, Nijdam W, Kuiper W S, Veldhuis G J, van Wolferen H and Elwenspoek M 1999 *J. Micromech. Microeng.* **9** 170
[3] Cao H, Yu Z, Wang J, Tegenfeldt J O, Austin R H, Chen E, Wu W and Chou S Y 2002 *Appl. Phys. Lett.* **81** 174
[4] Metz S, Trautmann C, Bertsch A and Renaud Ph 2004 *J. Micromech. Microeng.* **14** 324
[5] Venstra W J and Sarro P M 2003 *Microelectron. Eng.* **67** 502
[6] Stoenescu R and Meier W 2004 *Mol. Cryst. Liq. Cryst.* **417** 669
[7] Chen Y, Wang Z L, Yin J S, Johnson D J and Prince R H 1997 *Chem. Phys. Lett.* **272** 178
[8] Ren Z F, Huang Z P, Xu J W, Wang J H, Bush P, Siegal M P and Provencio P N 1998 *Science* **282** 1105
[9] Merkulov V I, Lowndes D H, Wei Y Y, Eres G and Voelkl E 2000 *Appl. Phys. Lett.* **76** 3555
[10] Ren Z F, Huang Z P, Wang D Z, Wen J G, Xu J W, Wang J H, Calvet L E, Chen J, Klemic J F and Reed M A 1999 *Appl. Phys. Lett.* **75** 1086
[11] Merkulov V I, Melechko A V, Guillorn M A, Lowndes D H and Simpson M L 2001 *Appl. Phys. Lett.* **79** 2970
[12] Melechko A V, Merkulov V I, McKnight T E, Guillorn M A, Klein K L, Lowndes D H and Simpson M L 2005 *J. Appl. Phys.* **97** 041301
[13] Fletcher B L, Hullander E D, Melechko A V, McKnight T E, Klein K L, Hensley D K, Morrell J L, Simpson M L and Doktycz M J 2004 *Nano Lett.* **4** 1809
[14] Zhang L, Melechko A V, Merkulov V I, Guillorn M A, Simpson M L, Lowndes D H and Doktycz M J 2002 *Appl. Phys. Lett.* **81** 135
[15] Carbonaro A, Walczak R, Calderale P M and Ferrari M 2004 *J. Membr. Sci.* **241** 249

[16] Kesting R E 1985 *Synthetic Polymeric Membranes, A Structural Perspective* 2nd edn (New York: Wiley)
[17] Mulder M 1999 *Basic Principle of Membrane Technology* (Dordrecht: Kluwer–Academic)
[18] Regan D G and Kuchel P W 2000 *Eur. Biophys. J.* **29** 221
[19] Leitner D M, Brown F L and Wilson K R 2000 *Biophys. J.* **78** 125
[20] Aliev M K and Tikhonov A N 2004 *Mol. Cell. Biochem.* **256/257** 257
[21] Suh J, Dawson M and Hanes J 2005 *Adv. Drug Delivery Rev.* **57** 63
[22] Hofman D, Fritz L, Ulbrich J and Paul D 1997 *Polymer* **38** 6145
[23] Falla W R, Mulski M and Cussler E 1996 *J. Membr. Sci.* **119** 129
[24] Lu S Y and Tsai C M 2000 *J. Membr. Sci.* **177** 55
[25] Grzywna Z J 1996 *Chem. Eng. Sci.* **51** 4115
[26] Liebovitch L S, Scheurle D, Rusek M and Zochowski M 2001 *Methods* **24** 359
[27] Merkulov V I, Hensley D K, Melechko A V, Guillorn M A, Lowndes D H and Simpson M L 2002 *J. Phys. Chem.* B **106** 10570